



Master's thesis
Astrophysical Sciences

Supermassive black holes and the cosmological formation of massive early-type galaxies (title not final)

Atte Keitaanranta

July 23, 2021

Supervisor(s): Prof. Peter Johansson
M.Sc. Matias Mannerkoski

Censor(s): Prof. Peter Johansson

UNIVERSITY OF HELSINKI
DEPARTMENT OF PHYSICS
PL 64 (Gustaf Hällströmin katu 2)
00014 University of Helsinki

Tiedekunta — Fakultet — Faculty	Koulutusohjelma — Utbildningsprogram — Education programme	
Faculty of Science	Department of Physics	
Tekijä — Författare — Author		
Atte Keitaanranta		
Työn nimi — Arbetets titel — Title		
Supermassive black holes and the cosmological formation of massive early-type galaxies (title not final)		
Opintosuunta — Studieinriktning — Study track		
Astrophysical Sciences		
Työn laji — Arbetets art — Level	Aika — Datum — Month and year	Sivumäärä — Sidoantal — Number of pages
Master's thesis	July 23, 2021	0 pages
Tiivistelmä — Referat — Abstract		
Abstract goes here.		
Avainsanat — Nyckelord — Keywords		
Your keywords here		
Säilytyspaikka — Förvaringsställe — Where deposited		
Muita tietoja — övriga uppgifter — Additional information		

Contents

1	Introduction	1
1.1	Information about galaxies, shortly	1
1.2	Aim of the thesis	1
2	Background	2
2.1	Cosmology	2
2.1.1	Hubble parameter, Friedmann equations and so on	2
2.1.2	Cosmological perturbations	2
2.2	Early-type galaxies	2
2.2.1	Types of ellipticals	2
2.2.2	Photometric and kinematic profiles	2
2.3	Evolution of dark matter halos	2
2.3.1	The Zel'Dovich approximation	2
2.4	Feedback processes	2
3	GADGET-3 and KETJU	3
3.1	Overview of GADGET-3	3
3.2	Smoothed Particle Hydrodynamics	3
3.3	Gas cooling?	3
3.4	Feedback?	3
3.5	KETJU	3

4 Creating initial conditions for the cosmological simulations	4
4.1 Zoom-in technique	4
4.2 MUSIC	6
4.2.1 Overview	6
4.2.2 Generation of the seed density field	7
4.2.3 Creation of nested grids	10
4.2.4 Particle displacements and velocity fields	13
4.3 Cosmological setup for the GADGET-3 zoom-in and KETJU simulations	14
4.4 Methods for locating regions of interest	15
4.4.1 Identifying halos: Friends-of-friends algorithm	16
4.4.2 Locating centers of objects: Shrinking sphere method	17
5 Cosmological GADGET-3 zoom-in simulations	18
5.0.1 Low-resolution run	18
5.1 Computational load of the simulations	18
5.2 Properties of the galaxies	18
5.2.1 Rotation curves	18
5.2.2 Star formation history	20
5.2.3 Colors and magnitudes	22
6 Simulations with KETJU	25
7 Conclusions	26
Bibliography	26

1. Introduction

1.1 Information about galaxies, shortly

1.2 Aim of the thesis

2. Background

2.1 Cosmology

2.1.1 Hubble parameter, Friedmann equations and so on

2.1.2 Cosmological perturbations

2.2 Early-type galaxies

2.2.1 Types of ellipticals

2.2.2 Photometric and kinematic profiles

2.3 Evolution of dark matter halos

2.3.1 The Zel'Dovich approximation

2.4 Feedback processes

3. GADGET-3 and KETJU

- Haven't really thought about the contents of this chapter yet

3.1 Overview of GADGET-3

3.2 Smoothed Particle Hydrodynamics

3.3 Gas cooling?

3.4 Feedback?

3.5 KETJU

4. Creating initial conditions for the cosmological simulations

This chapter describes how the initial conditions (ICs) for cosmological simulations are created. The first section describes the so-called 'zoom-in' method, which allows us to have spatially large simulation boxes with high resolution regions. After this, the code MUSIC (MULTi-Scale Initial Conditions) is introduced, which is used to create a spatial volume with realistic velocity and density perturbations at an early redshift ($z = 50$). Compared to an earlier implementation by Bertschinger (2001), the errors in the velocity and displacement fields are improved by two orders of magnitude (Hahn & Abel, 2011). The created initial ICs are used as a starting point for the performed GADGET-3 simulations that are run in this thesis. The last part of this chapter focuses on the setup of the cosmological setup of the simulations, and how the output of the preliminary low resolution large volume run is analyzed to find regions of interest needed for the higher resolution simulation.

4.1 Zoom-in technique

To study galaxy formation and evolution in a proper cosmological context, the simulation box must have a large volume. The perturbations at multiple fundamental length scales enter the non-linear regime at different redshifts and thus without a large enough volume (spatial dimensions of the box being $\sim 100 \text{ Mpc}$), the matter power spectrum is not resolved correctly on the largest scales. This results in unrealistic gravitational tidal forces from the large scale structures, which in turn create incorrect peculiar velocities in smaller scale structures, as shown in e.g. Mo et al. (2010).

To resolve the gravitational effects of a smaller scale structure, it is also required to have a high resolution, i.e. a large amount of particles with relatively low mass.

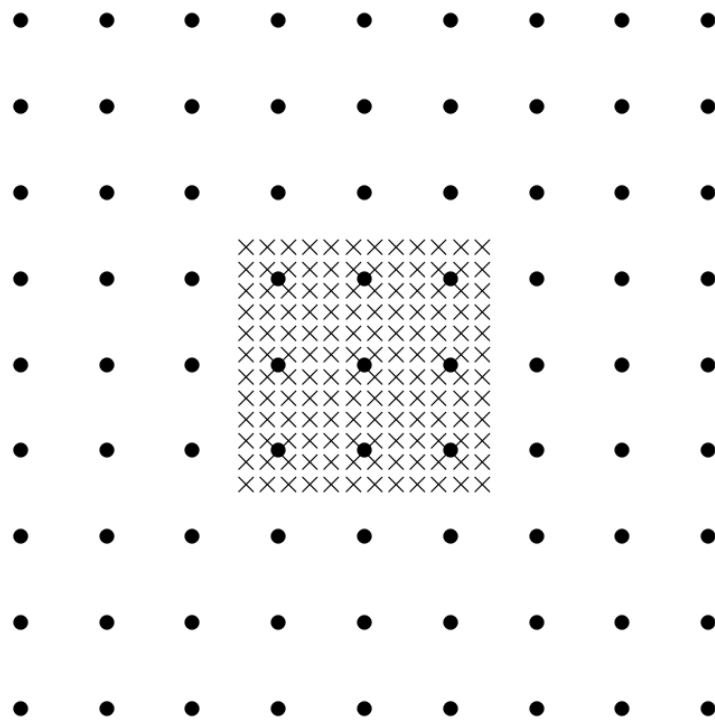


Figure 4.1: An example of a zoom-in region, with one level of mesh refinement. The circles represent the particles on the coarse grid. The crosses represent the refined particles, with each coarse particle inside this region divided into 4^3 particles (Bertschinger, 2001).

Having a sufficient resolution on the whole simulation volume would result in a unreasonably large computational workload. Thus it is more sensible to implement a method, which has a high resolution in a single region of interest, surrounded by a large volume with a smaller resolution. This method, nowadays known as the 'zoom-in' technique, has been in use for multiple decades. One of the first simulations with a region of interest surrounded by low resolution background was performed by Navarro & White (1994), and later implementations have been used by e.g. Power et al. (2003) and Marinacci et al. (2014) to name a few.

An example of a zoom-in grid is shown in Figure 4.1. Here, the dots represent the large particles on a coarse grid, while the crosses represent the refined grid with lower mass particles. In this refinement, each massive particle in the refined region is divided into 4^3 particles. Modern implementations, such as the one used in this thesis, use zoom regions with multiple levels of refinement (see Section 4.2.3). As adding levels of refinement resolves smaller structures, the results of zoom-in

simulations with different maximum resolution change slightly. The simulation with better resolution includes more low-mass satellites, and their locations can also differ. The masses of most massive objects are also affected, and mergers can occur at slightly different times.

To locate the regions of interest, we need to first perform a computationally less expensive simulation without a high resolution volume (discussed in 5.0.1) including only dark matter, and then choose the zoom-in regions and perform the simulation again with baryons included. The initial conditions (ICs) must also portray a realistic case, i.e. the fluctuations at a very high redshift must match the expected density structure from linear theory. As the redshift is till very high ($z > 20$), the evolution of density structures is still follows the linear theory. Fortunately, we can use a single program to create realistic ICs, with zoom-in box included.

4.2 Music

4.2.1 Overview

MUSIC (MULTI-Scale Initial Conditions) is a code written by Hahn & Abel (2011), which can be used to create the ICs for GADGET-3 simulations. The program creates a simulation volume, with velocity and particle displacements calculated using a power spectrum and two-point correlation given as input. To account for fluctuations on smaller scales, the program is also able to create a high resolution zoom-in region for the ICs. The zoom-in region can have multiple levels of refinement, and an example of an IC created using MUSIC is shown in Figure 4.2.

MUSIC improves on the prior work, e.g. the GRAFIC-2 code made by Bertschinger (2001), which also produces ICs with multiple levels of refinement. One of most notable upgrades in MUSIC compared to GRAFIC-2 is the way the transfer function is used to calculate the density perturbations, discussed in 4.2.2. Another improvement is the way different refinement levels constrain other levels, which is discussed in 4.2.3.

The initial conditions produced by the code best describe the velocity and density structure when the redshift of the produced ICs lie on the linear perturbation regime. If the initial redshift z_i of the ICs is set to be too low (i.e. on the non-linear regime), the formation of the first haloes occurs at unrealistically late times and the formation of high-mass haloes is suppressed, as shown by Reed et al. (2013). Still, MUSIC gives relatively accurate ICs even in the mildly non-linear regime of $z_i \sim 20$

(Hahn & Abel, 2011).

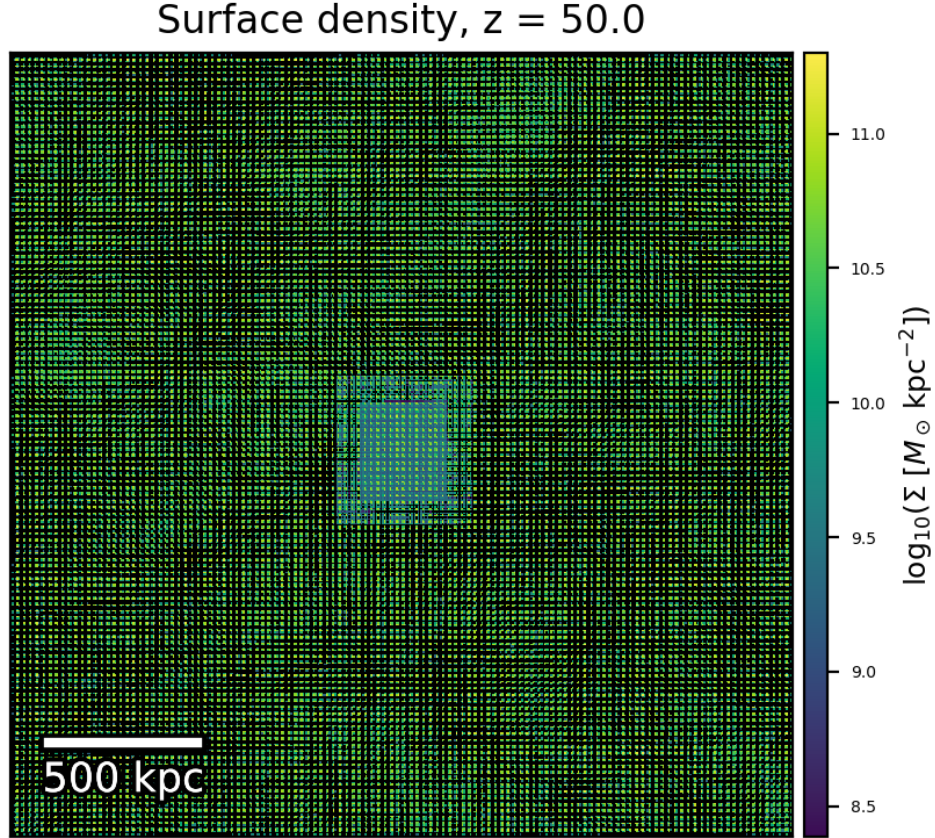


Figure 4.2: An example of a density field created using MUSIC, in physical units. The sidelength of the simulation box is 100 Mpc/h. At the center, a region with four refinement levels is included.

4.2.2 Generation of the seed density field

For the generation of particle velocities and positions, MUSIC first needs to create a density field, described by a density perturbation $\delta(\mathbf{r})$. Using an a Power spectrum $P(k)$ given as input, this field can be described completely, as the power spectrum of the field is given by

$$P(k) \equiv \langle \tilde{\delta}(\mathbf{k}) \tilde{\delta}^*(\mathbf{k}) \rangle, \quad (4.1)$$

where $*$ denotes the complex conjugate, and $\tilde{\delta}(\mathbf{k})$ represents the Fourier transform of the density perturbation, i.e.

$$\tilde{\delta}(\mathbf{k}) = \int \delta(\mathbf{x}) e^{-i\mathbf{k}\cdot\mathbf{x}} d^3\mathbf{x}. \quad (4.2)$$

The transfer function $T(k)$ can also be used to express the power spectrum, defined as

$$P(k) = \alpha k^{n_s} T^2(k), \quad (4.3)$$

where α is a constant used to normalize the power spectrum, and n_s is the spectral index, describing the slope of the spectrum. The value of the spectral index is given to MUSIC in the configuration file, while α is evaluated in using another, observable constant.

One way to normalize the spectrum is to measure the variance of the galaxy distribution σ^2 at a distance R . As shown in e.g. Mo et al. (2010), the predicted variance is defined as

$$\sigma^2(R) = \frac{1}{2\pi^2} \int P(k) \tilde{W}^2(k) k^2 dk, \quad (4.4)$$

where $\tilde{W}(k)$ is defined as the Fourier transform of a window function $W(r)$. There are multiple choices for the window function, and the most popular one is the top-hat window function $W(r)$, which is given by

$$W(r) = \begin{cases} \frac{3}{4\pi R^3}, & r \leq R \\ 0, & r > R. \end{cases} \quad (4.5)$$

The Fourier transform of this function is

$$\tilde{W}(k) = \frac{3}{(kR)^3} (\sin(kR) - kR \cos(kR)). \quad (4.6)$$

As the variance, as well as the shape of the power spectrum are known, the amplitude of the spectrum can now be normalized. For historical reasons, the distance where the variance is usually measured is $R = 8 \text{ Mpc}/\text{h}$, and is also the value MUSIC takes as input to normalize the power spectrum. At this distance, $\sigma(8 \text{ Mpc}/\text{h}) \equiv \sigma_8$ is valued close to unity. The value is close to one, since this is approximately the length scale at which the structure evolution becomes non-linear, with structures having higher length scales evolving linearly [SOURCE].

As the shape of the power spectrum are known and the spectrum is normalized, the generation of the density field is now possible. The goal is to create the density field from random noise values $\mu(\mathbf{r})$, while requiring that the amplitudes follow the power spectrum $P(k)$. The sample of random values $\mu(\mathbf{r})$ is called the white noise sample. White noise field is a field which with an constant power spectrum, i.e. $P(k) \propto k^n$ with $n = 0$ (Mo et al., 2010).

MUSIC generates the white noise sample using a Gaussian distribution. Detailed discussion of Gaussian distributions can be found in multiple sources of literature, for example Mo et al. (2010). For a distribution to be Gaussian, the probability density function ϱ of random value x is

$$\varrho(x) = \frac{1}{\sqrt{2\pi}\sigma} \exp\left(-\frac{(x - \bar{x})^2}{2\sigma^2}\right), \quad (4.7)$$

where \bar{x} and σ^2 are the mean and the variance, respectively. This equation can be generalized to higher dimensions, and for a n -dimensional random field $\delta(\mathbf{x}) = (\delta_1, \delta_2, \dots, \delta_n)$ the distribution is Gaussian if the probability distribution function can be written as

$$\varrho(\delta_1, \delta_2, \dots, \delta_n) = \frac{1}{\sqrt{(2\pi)^n \det(\mathcal{M})}} e^{-\mathcal{L}}, \quad (4.8)$$

where \mathcal{M} is the covariance matrix, $\mathcal{M}_{ij} = \langle \delta_i \delta_j \rangle$, and

$$\mathcal{L} \equiv \frac{1}{2} \sum_{i,j} \delta_i \left(\mathcal{M}^{-1} \right)_{ij} \delta_j. \quad (4.9)$$

It is assumed that the Gaussian random field is homogenous and isotropic, meaning that the multivariate Gaussian distribution functions are invariant under spatial translation or rotation. Therefore the two-point correlation function $\xi(r)$ completely determines the distribution functions. Specifically, the field's one-point distribution function is

$$\varrho(\delta) d\delta = \frac{1}{\sqrt{2\pi}\sigma^2} e^{-\frac{\delta^2}{2\sigma^2}} d\delta, \quad (4.10)$$

where the variance of the field is $\langle \delta^2(\mathbf{x}) \rangle = \sigma^2 = \xi(0)$. Note: Peter, you mentioned that I should explain a bit what $\xi(0)$ means, but I'm struggling with this. Is there a book/paper I could check or could you explain a bit what $\xi(0)$ means?

Returning to the white noise sample, the amplitudes of the random values $\mu(\mathbf{r})$ can be generated to follow the power spectrum $P(k)$ by considering the Fourier transformed random field $\tilde{\mu}(\mathbf{k})$. With this, the Fourier transformed field $\tilde{\delta}(\mathbf{k})$ can be written as

$$\tilde{\delta}(\mathbf{k}) = \sqrt{P(||\mathbf{k}||)} \tilde{\mu}(\mathbf{k}) = \alpha ||\mathbf{k}||^{n_s/2} T(||\mathbf{k}||) \tilde{\mu}(\mathbf{k}). \quad (4.11)$$

A common procedure to evaluate the real-space density field is to perform an inverse Fourier transform to $\tilde{\delta}(\mathbf{k})$, as is done in e.g. Bertschinger (2001). MUSIC uses a different approach, and calculates the real-space density field as

$$\delta(\mathbf{r}) = \mathcal{T}_R(||\mathbf{r}||) * \mu(\mathbf{r}), \quad (4.12)$$

where $\mathcal{T}_R(r)$ is the real-space counterpart of $\tilde{\mathcal{T}}(k) \equiv \alpha k^{n_s/2} T(k)$ and "*" is denoting a convolution, discussed thoroughly by Salmon (1996). Briefly, the white noise $\mu(\mathbf{x})$ is realised as density perturbations in real space using the convolution operator. This method has previously been used by e.g. Pen (1997) and Sirk (2005). Hahn & Abel (2011) also show that previous implementations that use the inverse Fourier transform of $\delta(\mathbf{k})$ results in too small values for the two-point correlation function.

To calculate the $\delta(\mathbf{r})$ via convolution, it is till required to transform $\tilde{\mathcal{T}}(k)$ into real space, which MUSIC achieves by performing the calculation (assuming that $\tilde{\mathcal{T}}(k)$ is spherically symmetric)

$$\mathcal{T}_R(r) = \frac{1}{(2\pi)^3} \int_{\mathbb{R}} \tilde{\mathcal{T}}(k) e^{i\mathbf{x} \cdot \mathbf{k}} \cdot \mathbf{k} d^3 \mathbf{k} \quad (4.13)$$

$$= \frac{1}{2\pi^2} \int_0^\infty \tilde{\mathcal{T}}(k) \frac{\sin(kr)}{kr} dk. \quad (4.14)$$

4.2.3 Creation of nested grids

When creating the refined regions, the white noise of the subgrids must be consistent with the white noise og the coarse domain, meaning that when dividing a particle (parent cell) into smaller particles (children cells), the mass must be conserved. A common way to achieve this has been the Hofmann-Ribak algorithm (Hoffman & Ribak, 1991), which GRAFIC-2 also uses.

The Hofmann-Ribak algorithm first creates individually white noise fields w^ℓ and $w^{\ell+1}$. The field with higher level of refinement is unconstrained at this point and has a variance 8 times higher than the one level coarses ℓ . Having 8 times higher variance is equivalent to dividing the parent cells into groups eight children cells. To match the level $\ell + 1$ to ℓ , the mean white noise of the finer level must be matched to the value of the coarser level. Bertschinger (2001) achieves this by subtracting the mean of the unconstrained sample from the sum of the coarse white noise and the unconstrained white noise.

While this algorithm does conserve the mass of the coarse grid on the finer subgrids, the approach does not preserve the Fourier modes of the coarse white noise. Thus MUSIC uses a modified method, which still utilizes the Hofmann-Ribak algorithm while retaining the Fourier modes.

When creating the refined subgrids, the method still divides each parent cell into eight children cells. A two-dimensional example of this is shown in Figure 4.3. After this, the Fourier modes of the coarse grid are preserved by performing a Fast Fourier Transform (FFT) of the transfer function on two regions: on the fine grid,

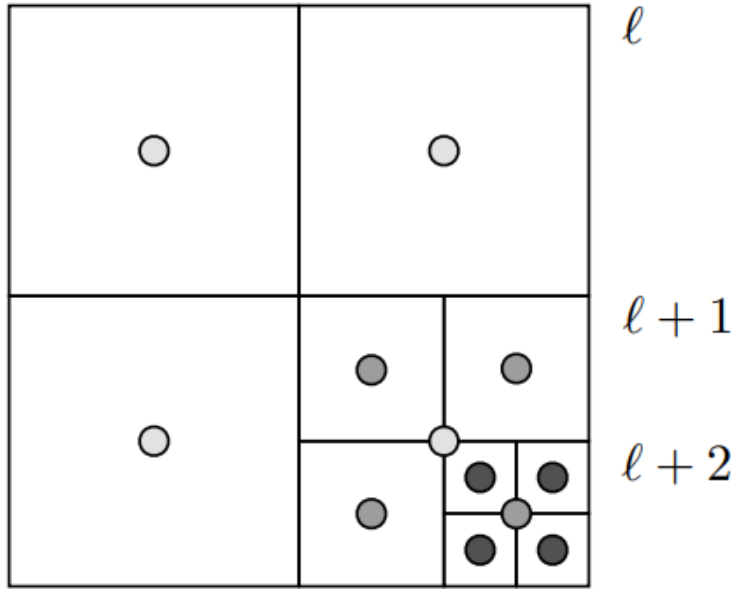


Figure 4.3: A two dimensional example layout of multiple scale nested grid (Hahn & Abel, 2011). The figure shows parent cells on level ℓ , and children cells on two higher levels. The center of the children cells is not in the same position as the center of the parent cell.

and on the coarse grid region which is overlapping with the finer grid. For the finer grid, all of the modes up to the so-called Nyquist wave of the coarse grid, $\mathbf{k} \leq \mathbf{k}_{Ny}$, are then replaced by with the modes of the coarse level. The value of the Nyquist wave number is $k_{Ny} = \pi / \Delta x$, where Δx is the spacing of the particles on the coarse grid. This value acts as a cutoff value for the FFT, as numerical calculations of Fourier transformations cannot be continued to infinity.

The Fourier modes are now preserved, and an inverse Fourier transform can be performed to create the a refined subgrid with perserved Fourier modes. Finally, a reverse version of the Holffmann-Ribak algorithm is used. With this, average of the children cells on the finer level define and replace the the white noise values of the coarser level on the overlapping regions.

With multiple levels of refined subgrids present, this method is started from the finest subgrid, and moving to coarser grids one level at a time. In the regions where levels ℓ and $\ell + 1$ overlap, the parent cells are replaced by the average of the eight children cells and thus, in addition to conserving the Fourier modes, the mass is conserved.

To calculate the over-density fields on each level of the nested grids using FFTs, the convolution kernels $T(r)$ are still needed for all refined levels. For this, the levels

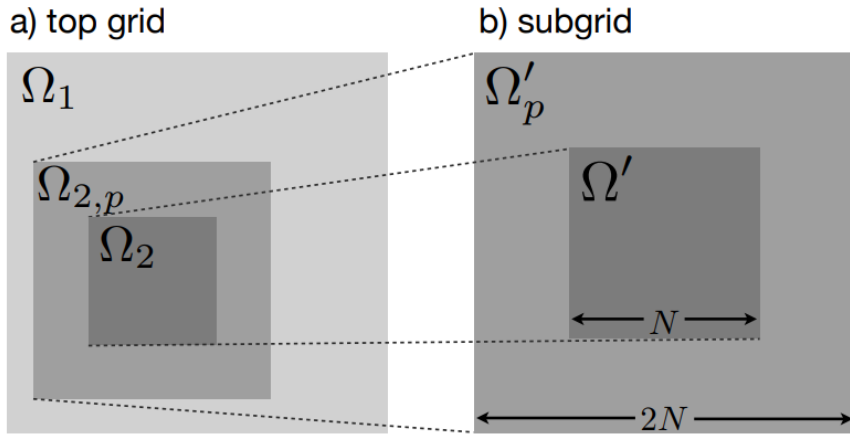


Figure 4.4: A two-dimensional representation of domains of two levels of refinement, including the padded domain for the subgrid. The domain of the higher resolution level has a sidelength of N , and the padded domain has a sidelength of $2N$ (Hahn & Abel, 2011).

of the nested grid are divided into domains Ω_ℓ and each domain is surrounded by a padded domain $\Omega_{\ell,p}$. The sides of the padded domain are double the length compared to the domain Ω_ℓ , as shown in Figure 4.4. The padded domain is needed to keep the Fourier transforms isolated, which leads to conservation of the wave modes when performing the convolution.

The creation of convolution kernels starts from the finest level ℓ . At this level, the convolution kernel in the domain and the padded domain is simply equivalent to the real-space transfer function,

$$T^\ell(\mathbf{x}) = \mathcal{T}_R(||\mathbf{x}||), \quad (4.15)$$

where \mathcal{T}_R is evaluated as shown in eq. 4.14. The origin is placed at the center of the domain. For the next level, the calculation of the kernel is performed in two different ways, depending on the location for which the kernel is evaluated at. If the location on the level does not have a refined subgrid over it, the calculation for the kernel is performed in the same way as for the most refined level, as shown in eq. 4.15. As mentioned before, for the overlapping regions, the kernels all averaged over the eight children cells. This is achieved with the calculation

$$T^{\ell-1}(\mathbf{x}) = T^{\ell-1}(x, y, z) = \frac{1}{8} \sum_{i,j,k \in \{-\frac{\Delta x^\ell}{2}, \frac{\Delta x^\ell}{2}\}} T^\ell(x + i, y + j, z + k), \quad (4.16)$$

where Δx^ℓ is the spacing of the particles on level ℓ . The relation of the spacing of particles in refinement levels ℓ and $\ell - 1$ is $\Delta x^{\ell-1}/\Delta x^\ell = 2$. After level $\ell - 1$, the

calculation of kernels moves on to level $\ell - 2$, and so on. For these, the kernels are calculated the same way as for level $\ell - 1$.

4.2.4 Particle displacements and velocity fields

Note: I'll explain more about the Zeldovich approximation on chapter 2

The generated density field from the white noise sample is used as a starting point for the evolution of particle position and velocity fields. The evolution is calculated using the Lagrangian perturbation theory. Time evolution of position and velocity of each fluid element (i.e. each particle) is followed until the initial redshift z_i is reached. The time evolution of the density field "displaces" particles, turning the initial Gaussian field into a non-Gaussian field.

In Lagrangian perturbation theory, the time evolution of position $\mathbf{x}(t)$ and velocity $\mathbf{v}(t)$ is determined by a so-called "displacement field" $\mathbf{L}(\mathbf{q}, t)$, where \mathbf{q} is the initial position of a particle. The time evolution of position and velocity is written as

$$\mathbf{x}(t) = \mathbf{q} + \mathbf{L}(\mathbf{q}, t), \quad (4.17)$$

$$\mathbf{v}(t) = \frac{d\mathbf{L}(\mathbf{q}, t)}{dt}. \quad (4.18)$$

For the numerical calculation of the displacement field, MUSIC uses the first order approximation, the so-called Zel'Dovich approximation (Zel'Dovich (1970), see also 2.3.1). With this, the displacement field can be calculated as

$$\mathbf{L}(\mathbf{q}, t) = -\frac{2}{3H_0^2 a^2 D(t)} \nabla \phi(\mathbf{q}, t) \equiv D^{-1}(t) \nabla \Phi(\mathbf{q}, t), \quad (4.19)$$

where $D(t)$ is the growth factor of linear density perturbations and Φ is the potential, whose gradient is proportional to the gradient of the gravitational potential ϕ (Hahn & Abel, 2011). The evolution of the gravitational potential is calculated by solving the Poisson's equation, which is written as

$$\Delta \phi(\mathbf{q}, t) = \frac{3}{2} H_0^2 a^2 \delta(\mathbf{q}, t). \quad (4.20)$$

With this first order approximation, the velocity of each particle is acquired via a gradient of the potential. Thus the velocity field with this approximation results in $\nabla \times \mathbf{v}(t) = 0$ (Hahn & Abel, 2011). MUSIC is also capable of calculating the fields using a more complicated second order approximation, but it was not used when generating ICs for the simulations in this thesis.

To achieve a numerical solution for the Poisson's equation, MUSIC uses a hybrid of two methods, FFT and a multi-grid solution called Full Approximation Scheme (FAS, Brandt (1977)), solving the equation on the finest grid and proceeding from that to coarser levels. With this hybrid method, the FFT is only used for the finest level.

For the levels in which the Poisson's equation is solved using FAS, the equation is written in the form of

$$\Delta\phi(\mathbf{x}) = f(\mathbf{x}). \quad (4.21)$$

The implementation of FAS in MUSIC is thoroughly explained in the paper by Hahn & Abel (2011). In summary, MUSIC approximates the value of ϕ on grid level ℓ to be u^ℓ , with the operator Δ being approximated to Laplacian value L , taken from a table. These can be used to calculate the residual term $r^\ell = f^\ell - L^\ell u^\ell$. This generates two terms affecting level $\ell - 1$. The second term generates an additional correction term for the grid at level $\ell - 1$. In addition, a restrictive term is present due to the first source term, f^ℓ . To account for these terms, a so-called smoothing scheme $S(u^\ell, f^\ell)$ is performed, and is applied using the Gauss-Seidel sweep. This method is applied recursively on each level to decrease the value of the residual r^ℓ until a threshold value is reached, resulting in an excellent approximation for the value of ϕ and allowing the program to create the necessary ICs for cosmological simulations.

4.3 Cosmological setup for the GADGET-3 zoom-in and KETJU simulations

The goal of this thesis is to study the output of cosmological simulations performed with GADGET-3 and KETJU. To acquire the simulation data analyzed in chapters 5 and 6, the following steps and runs are performed:

1. Generate an IC without baryons using MUSIC.
2. Run a GADGET-3 simulation from the created IC to redshift $z = 0$.
3. Locate areas of interest from the output.
4. Use MUSIC to create ICs with zoom-in regions. Two versions are created: with and without baryons.
5. Perform the zoom-in cosmological runs with GADGET-3.

6. Analyze the output data and starting points for simulations with KETJU enabled.
7. Perform the KETJU runs and analyze the data.

All of the performed simulations use the same cosmological parameters, which are shown in Table 4.1, also including the resulting critical density. These are the default values MUSIC uses, and are very close to observed estimates (Planck Collaboration et al., 2020). In addition, all of the simulations have periodic boundary conditions. The starting redshift of the ICs created with MUSIC is set to $z_i = 50$ and the sidelength of the box is set to 100 Mpc/h.

H_0 (km/s/Mpc)	Ω_m	Ω_b	Ω_Λ	σ_8	n_s	ρ_{crit} (kg/m ³)
70.3	0.276	0.045	0.724	0.811	0.961	9.28×10^{-27}

Table 4.1: Cosmological parameters used for the simulations. The critical density acquired with these parameters is also included. If a simulation doesn't include baryons, the dark matter density parameter Ω_{DM} is equal to the matter density parameter Ω_m . If baryons are included, $\Omega_{\text{DM}} = \Omega_m - \Omega_b$.

The coarse grid is made up of 128^3 particles. The matter density can be written as

$$\rho_m = \Omega_m \rho_{\text{crit}} = \frac{Nm}{V}, \quad (4.22)$$

where N is the number of particles, m the mass of a single particle and $V = L^3$ is the volume of the box. Combining this with the equation for critical density (eq. 2.??, added after chapter 2 is written), the mass of a single particle can be calculated with

$$m = \frac{V}{N} \Omega_m \rho_{\text{crit}} = \frac{L^3}{N} \frac{3H(t)^2}{8\pi G} \Omega_m. \quad (4.23)$$

For the simulations performed here, this leads to coarsest particles having a mass of $3.65 \times 10^{10} M_\odot/h$.

4.4 Methods for locating regions of interest

For the analysis of the cosmological simulations (and to locate regions of interest for the zoom-in simulations), an algorithm is needed to locate halos from the low resolution dark matter only simulation (discussed in 5.0.1). Here, two methods are shortly introduced. The first is used to divide the simulation particles into groups, each being a halo. The second method is used to find a center of mass of a halo, necessary for the analysis of the formed halos and galaxies.

4.4.1 Identifying halos: Friends-of-friends algorithm

To divide the output data into objects, an algorithm called the Friends-of-Friends (FoF) algorithm is used. Versions of the algorithm have been used for observational surveys and simulation data, e.g. Huchra & Geller (1982) and Nolthenius & White (1987) for survey implementations Davis et al. (1985) and Nurmi et al. (2013) for usage with simulation data, to name a few.

To use the algorithm on the output data, a Python module pygad (Röttgers et al., 2020) is used. With this, the FoF algorithm is used to divide the simulation particles into groups, with each group representing a halo. A particle is considered to be a part of the same group as another particle, if the distance between the two particles is smaller than a determined threshold value l . This value is often called the linking length and these two particles are called ‘friends’. Similarly, two particles in two individual groups are separated by a length smaller than the linking length, the two groups are combined to one group. An example of two groups defined with FoF is shown in Figure 4.5.

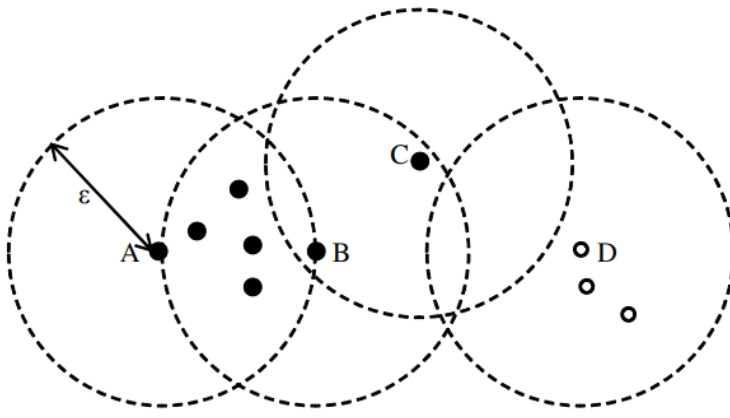


Figure 4.5: An example showing two groups defined with the FoF algorithm, as shown in Kwon et al. (2010). Black particles form one group, and the white ones another. For particles A, B, C and D, circles having a radius ϵ , which is equal to the linking length is shown. Particles inside the circles are the friends of the central particle. For example, even though particles A and C are not considered friends, they are still part of the same group.

The FoF algorithm is used to find objects using the position of dark matter particles. However, the determined groups do not necessarily represent physical, gravitationally bound structures. Thus the center of a determined group may not coincide with the center of the halo, and another after applying the FoF algorithm, another method is used to locate the centers.

4.4.2 Locating centers of objects: Shrinking sphere method

The centers of the objects defined with the FoF algorithm are calculated with the so-called shrinking sphere method (Power et al., 2003). This method is also applied using pygad (Röttgers et al., 2020).

The method begins with placing a sphere with radius r_0 around the center location of object determined using the FoF algorithm. The new location of the calculated center is then placed at the center of mass of the particles within the sphere. Another, shrunken sphere is then placed at this location with the radius being a few percent smaller than the previous radius. In this thesis, the radius is shrunk by 2.5%.

To find the real center of the object, this method is applied recursively. After each placement of a shrunken sphere, new center of mass is calculated using the particles within the new sphere. These steps are applied recursively until the amount of particles left inside a sphere decreases below a threshold limit. The real center is the final center of mass calculated. Acquiring a great estimate for the center makes it possible to analyse multiple properties of the formed halos and galaxies, like colors and rotations curves, for example.

5. Cosmological GADGET-3 zoom-in simulations

5.0.1 Low-resolution run

- Conditions of the chosen halos
- Figure showing the zoom-in regions from the low res run

5.1 Computational load of the simulations

- Quick overview: CPUs used, time elapsed, where simulations were run

5.2 Properties of the galaxies

Simulation	r_{vir} (kpc)	M_* (M_\odot)	M_V (mag)	$M_{*,\text{gal}}/M_{\text{vir}}$	M_{bh} (M_\odot)
Med res, A	517	3.98×10^{11}	-22.4	0.025	5.82×10^9
Med res, B	574	5.16×10^{11}	-22.7	0.024	6.23×10^9
Med res, C	400	2.56×10^{11}	-22.0	0.035	3.96×10^9
High res, A	526	5.31×10^{11}	-22.6	0.032	3.64×10^9
High res, B	578	6.38×10^{11}	-22.8	0.029	4.54×10^9
High res, C	400	3.46×10^{11}	-22.2	0.047	2.80×10^9

Table 5.1: Properties of the zoomed-in galaxies at redshift $z = 0$.

5.2.1 Rotation curves

- Med res galaxy A simulation is performed with single precision, I'm currently doing the simulation in double precision

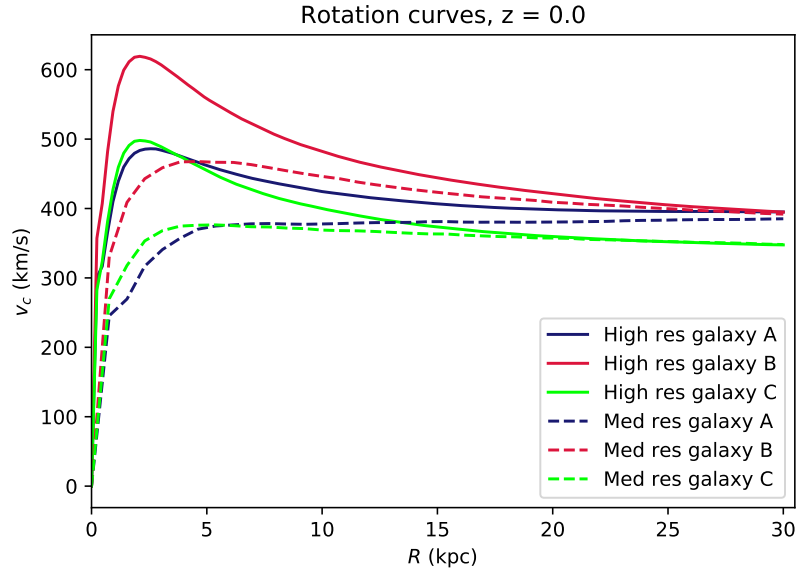


Figure 5.1: Rotation curves for each galaxy including baryons, at redshift 0. The continuous lines represent the high resolution simulations and the dasheld lines represent the medium resolution simulations.

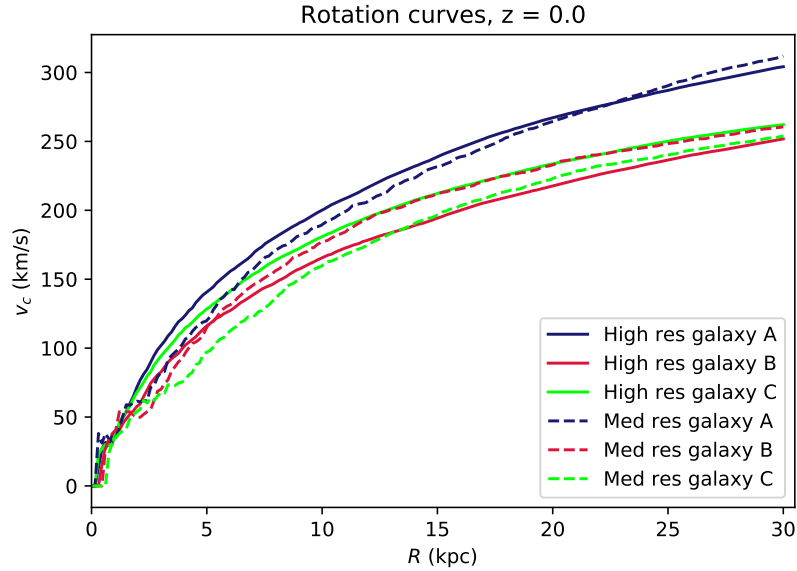


Figure 5.2: Rotation curves for each galaxy including only dark matter, at redshift 0. The continuous lines represent the high resolution simulations and the dasheld lines represent the medium resolution simulations.

- Rotation curves do not have the same limits on the y-axis

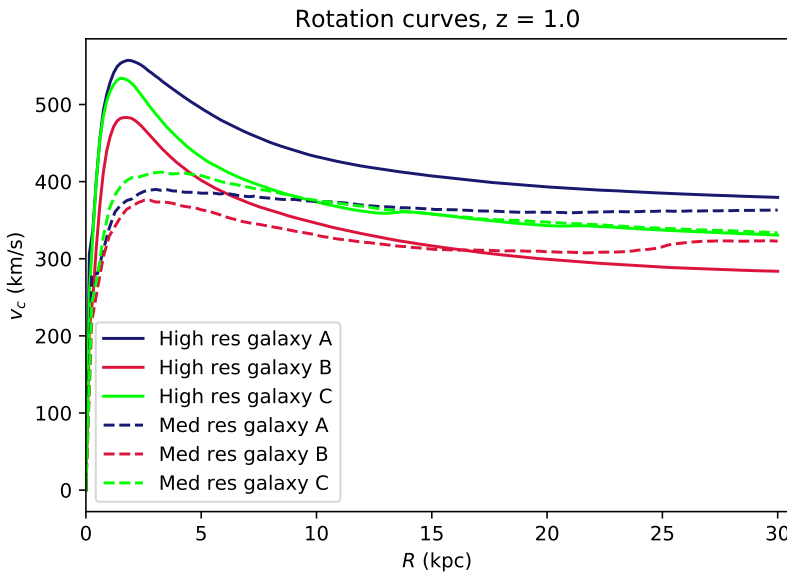


Figure 5.3: Rotation curves for each galaxy including baryons, at redshift 1. The continuous lines represent the high resolution simulations and the dasheld lines represent the medium resolution simulations.

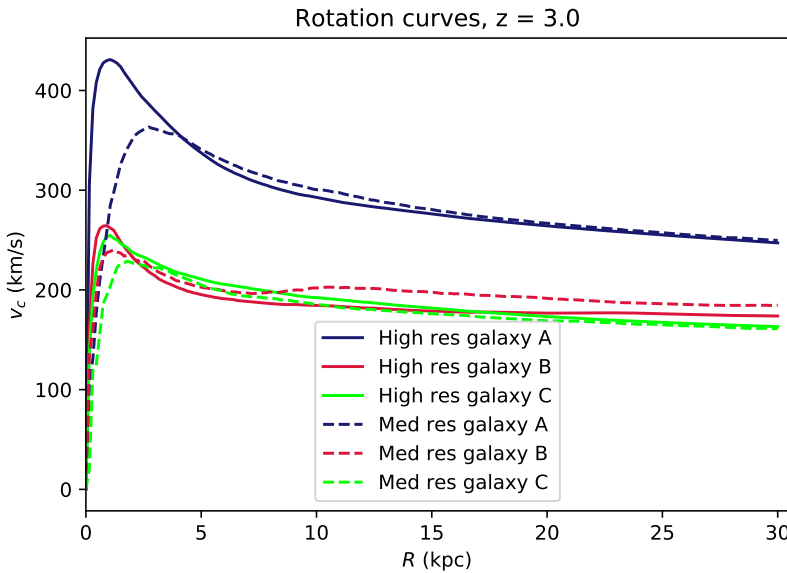


Figure 5.4: Rotation curves for each galaxy including baryons, at redshift 3. The continuous lines represent the high resolution simulations and the dasheld lines represent the medium resolution simulations.

5.2.2 Star formation history

- The stellar mass evolution plot is not yet done for high res simulations.

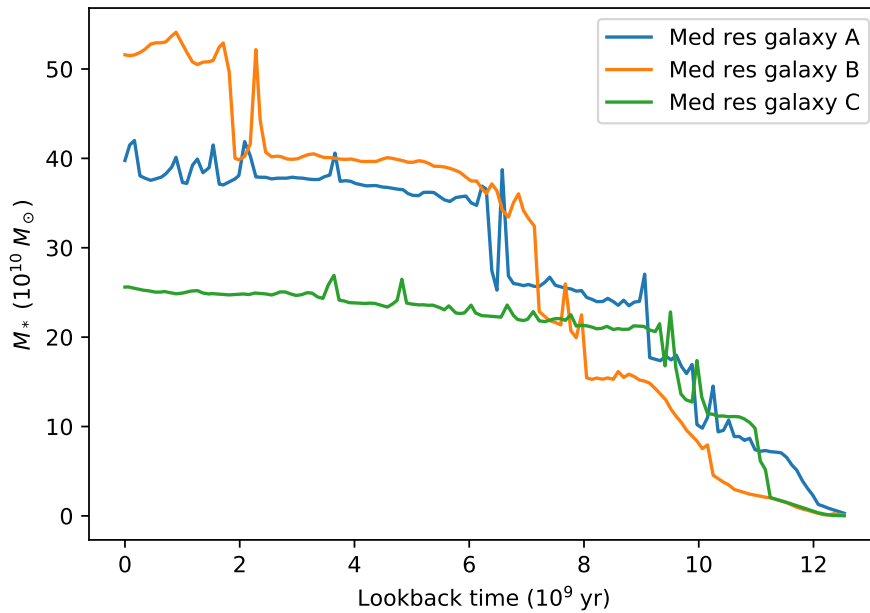


Figure 5.5: Stellar mass evolution for the medium resolution galaxies. The calculated stellar mass is the stellar mass within $r_{\text{gal}} = r_{\text{vir}}/10$.

- Redshifts missing from the stellar mass evolution plot
- SFRs, also histograms?
- Again, med res A results will probably change a bit when double precision run is finished.
- Formation efficiencies, comparing to the cosmological parameter

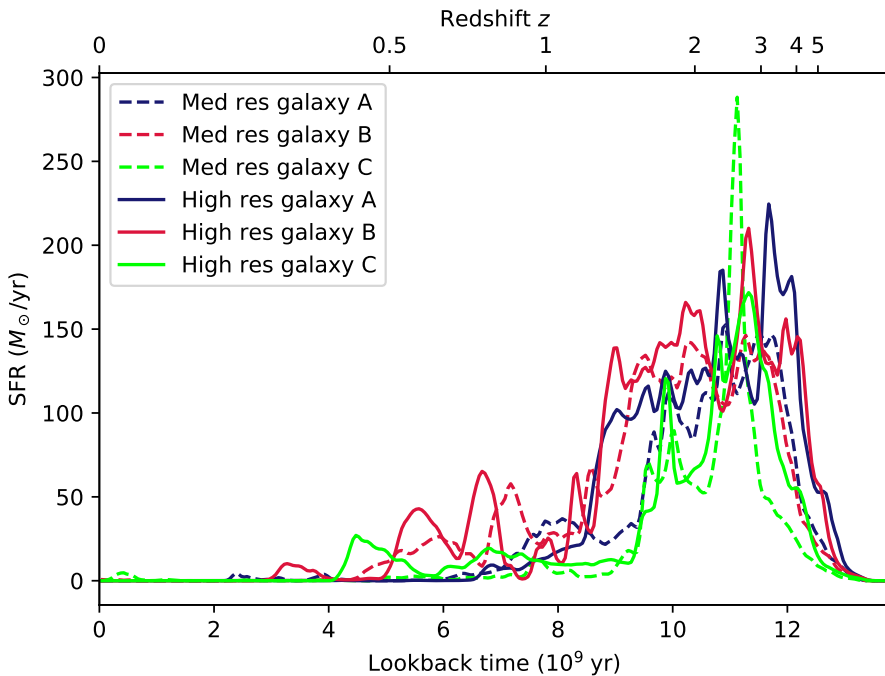


Figure 5.6: Stellar formation rates for each zoomed-in galaxy, plotted as a function of lookback time. The lines are created from histograms having a length of 5 Myr, which are then smoothed. The continuous lines represent the high resolution simulations and the dashed lines represent the medium resolution simulations.

5.2.3 Colors and magnitudes

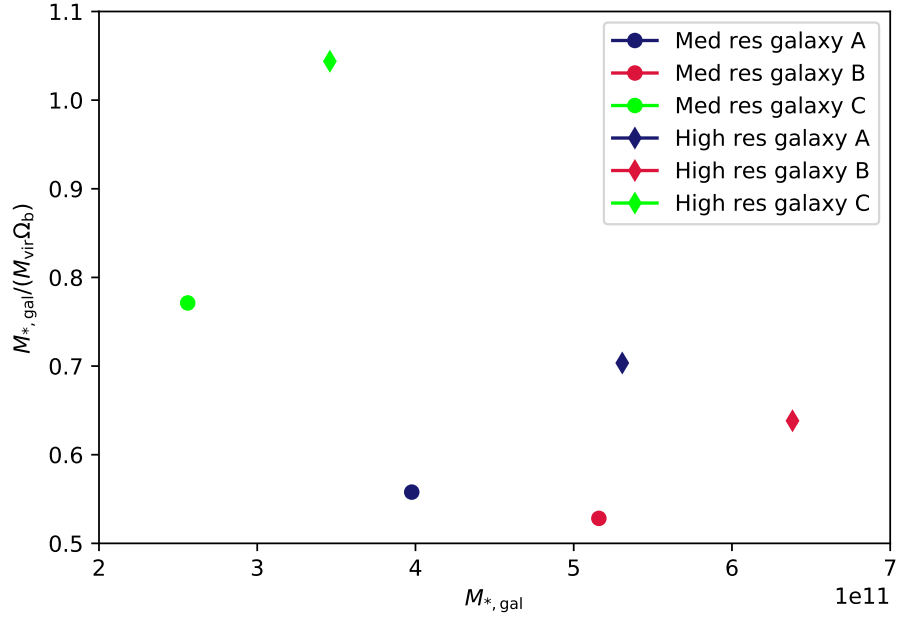


Figure 5.7: Galaxy formation efficiencies for each galaxy, plotted with their stellar masses. The cosmological baryon density Ω_b is set to 0.045 in the simulations. The diamond and circular markers show the results of the high resolution and the medium resolution zoom-in simulations, respectively.

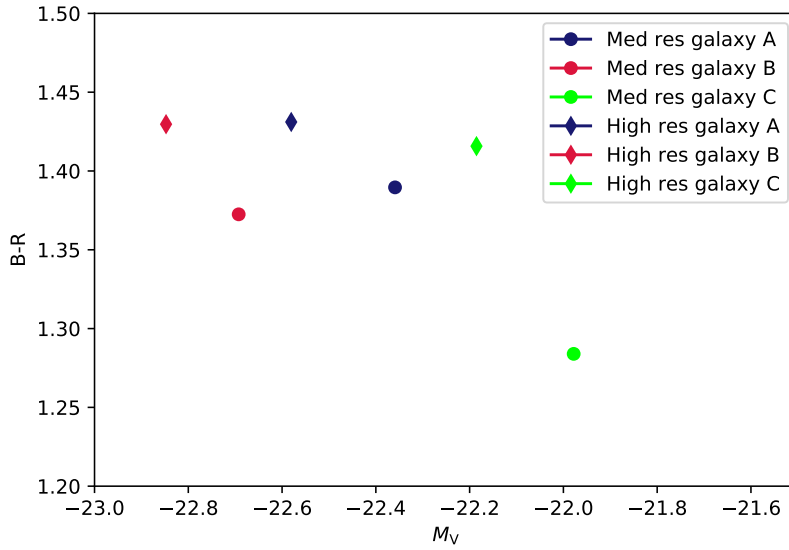


Figure 5.8: B-R colors for each simulated galaxy, plotted with each galaxy's absolute magnitude in the V-band. The diamond and circular markers show the results of the high resolution and the medium resolution zoom-in simulations, respectively.

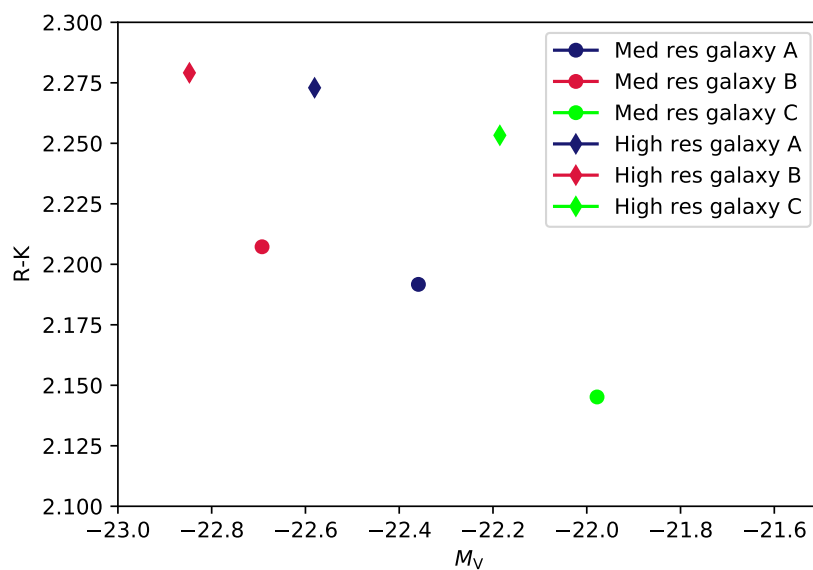


Figure 5.9: R-K colors for each simulated galaxy, plotted with each galaxy's absolute magnitude in the V-band. The diamond and circular markers show the results of the high resolution and the medium resolution zoom-in simulations, respectively.

6. Simulations with KETJU

7. Conclusions

- recap on what was written/studied
- more own thoughts on results
- future missions
- how could the simulations be more realistic (higher resolution, more feedback stuff?)

Bibliography

- Bertschinger, E. (2001). Multiscale Gaussian Random Fields and Their Application to Cosmological Simulations. *Astrophysical Journal Supplement Series*, 137(1):1–20.
- Brandt, A. (1977). Multi-level adaptive solutions to boundary-value problems. *Mathematics of Computation*, 31(138):333–390.
- Davis, M., Efstathiou, G., Frenk, C. S., & White, S. D. M. (1985). The evolution of large-scale structure in a universe dominated by cold dark matter. *Astrophysical Journal*, 292:371–394.
- Hahn, O. & Abel, T. (2011). Multi-scale initial conditions for cosmological simulations. *Monthly Notices of the Royal Astronomical Society*, 415(3):2101–2121.
- Hoffman, Y. & Ribak, E. (1991). Constrained Realizations of Gaussian Fields: A Simple Algorithm. *Astrophysical Journal Letters*, 380:L5.
- Huchra, J. P. & Geller, M. J. (1982). Groups of Galaxies. I. Nearby groups. *Astrophysical Journal*, 257:423–437.
- Kwon, Y., Nunley, D., Gardner, J. P., Balazinska, M., Howe, B., & Loebman, S. (2010). Scalable clustering algorithm for n-body simulations in a shared-nothing cluster. In Gertz, M. & Ludäscher, B., editors, *Scientific and Statistical Database Management*, page 132–150. Springer Berlin Heidelberg.
- Marinacci, F., Pakmor, R., & Springel, V. (2014). The formation of disc galaxies in high-resolution moving-mesh cosmological simulations. *Monthly Notices of the Royal Astronomical Society*, 437(2):1750–1775.
- Mo, H., van den Bosch, F. C., & White, S. (2010). *Galaxy Formation and Evolution*.
- Navarro, J. F. & White, S. D. M. (1994). Simulations of dissipative galaxy formation in hierarchically clustering universes-2. Dynamics of the baryonic component in

- galactic haloes. *Monthly Notices of the Royal Astronomical Society*, 267(2):401–412.
- Nolthenius, R. & White, S. D. M. (1987). Groups of galaxies in the CfA survey and in cold dark matter universes. *Monthly Notices of the Royal Astronomical Society*, 225:505–530.
- Nurmi, P., Heinämäki, P., Sepp, T., Tago, E., Saar, E., Gramann, M., Einasto, M., Tempel, E., & Einasto, J. (2013). Groups in the Millennium Simulation and in SDSS DR7. *Monthly Notices of the Royal Astronomical Society*, 436(1):380–394.
- Pen, U.-L. (1997). Generating Cosmological Gaussian Random Fields. *Astrophysical Journal Letters*, 490(2):L127–L130.
- Planck Collaboration, Aghanim, N., Akrami, Y., Ashdown, M., Aumont, J., Bacigalupi, C., Ballardini, M., Banday, A. J., Barreiro, R. B., Bartolo, N., Basak, S., Battye, R., Benabed, K., Bernard, J. P., Bersanelli, M., Bielewicz, P., Bock, J. J., Bond, J. R., Borrill, J., Bouchet, F. R., Boulanger, F., Bucher, M., Burigana, C., Butler, R. C., Calabrese, E., Cardoso, J. F., Carron, J., Challinor, A., Chiang, H. C., Chluba, J., Colombo, L. P. L., Combet, C., Contreras, D., Crill, B. P., Cuttaia, F., de Bernardis, P., de Zotti, G., Delabrouille, J., Delouis, J. M., Di Valentino, E., Diego, J. M., Doré, O., Douspis, M., Ducout, A., Dupac, X., Dusini, S., Efstathiou, G., Elsner, F., Enßlin, T. A., Eriksen, H. K., Fantaye, Y., Farhang, M., Fergusson, J., Fernandez-Cobos, R., Finelli, F., Forastieri, F., Frailis, M., Fraisse, A. A., Franceschi, E., Frolov, A., Galeotta, S., Galli, S., Ganga, K., Génova-Santos, R. T., Gerbino, M., Ghosh, T., González-Nuevo, J., Górski, K. M., Gratton, S., Gruppuso, A., Gudmundsson, J. E., Hamann, J., Handley, W., Hansen, F. K., Herranz, D., Hildebrandt, S. R., Hivon, E., Huang, Z., Jaffe, A. H., Jones, W. C., Karakci, A., Keihänen, E., Kesktalo, R., Kiiveri, K., Kim, J., Kisner, T. S., Knox, L., Krachmalnicoff, N., Kunz, M., Kurki-Suonio, H., Lagache, G., Lamarre, J. M., Lasenby, A., Lattanzi, M., Lawrence, C. R., Le Jeune, M., Lemos, P., Lesgourgues, J., Levrier, F., Lewis, A., Liguori, M., Lilje, P. B., Lilley, M., Lindholm, V., López-Caniego, M., Lubin, P. M., Ma, Y. Z., Macías-Pérez, J. F., Maggio, G., Maino, D., Mandolesi, N., Mangilli, A., Marcos-Caballero, A., Maris, M., Martin, P. G., Martinelli, M., Martínez-González, E., Matarrese, S., Mauri, N., McEwen, J. D., Meinhold, P. R., Melchiorri, A., Menella, A., Migliaccio, M., Millea, M., Mitra, S., Miville-Deschénes, M. A., Molinari, D., Montier, L., Morgante, G., Moss, A., Natoli, P., Nørgaard-Nielsen, H. U.,

- Pagano, L., Paoletti, D., Partridge, B., Patanchon, G., Peiris, H. V., Perrotta, F., Pettorino, V., Piacentini, F., Polastri, L., Polenta, G., Puget, J. L., Rachen, J. P., Reinecke, M., Remazeilles, M., Renzi, A., Rocha, G., Rosset, C., Roudier, G., Rubiño-Martín, J. A., Ruiz-Granados, B., Salvati, L., Sandri, M., Savelainen, M., Scott, D., Shellard, E. P. S., Sirignano, C., Sirri, G., Spencer, L. D., Sunyaev, R., Suur-Uski, A. S., Tauber, J. A., Tavagnacco, D., Tenti, M., Toffolatti, L., Tomasi, M., Trombetti, T., Valenziano, L., Valiviita, J., Van Tent, B., Vibert, L., Vielva, P., Villa, F., Vittorio, N., Wandelt, B. D., Wehus, I. K., White, M., White, S. D. M., Zacchei, A., & Zonca, A. (2020). Planck 2018 results. VI. Cosmological parameters. *Astronomy & Astrophysics*, 641:A6.
- Power, C., Navarro, J. F., Jenkins, A., Frenk, C. S., White, S. D. M., Springel, V., Stadel, J., & Quinn, T. (2003). The inner structure of Λ CDM haloes - I. A numerical convergence study. *Monthly Notices of the Royal Astronomical Society*, 338(1):14–34.
- Reed, D. S., Smith, R. E., Potter, D., Schneider, A., Stadel, J., & Moore, B. (2013). Towards an accurate mass function for precision cosmology. *Monthly Notices of the Royal Astronomical Society*, 431(2):1866–1882.
- Röttgers, B., Naab, T., Cernetic, M., Davé, R., Kauffmann, G., Borthakur, S., & Földl, H. (2020). Lyman α absorption beyond the disc of simulated spiral galaxies. *Monthly Notices of the Royal Astronomical Society*, 496(1):152–168.
- Salmon, J. (1996). Generation of Correlated and Constrained Gaussian Stochastic Processes for N-Body Simulations. *Astrophysical Journal*, 460:59.
- Sirko, E. (2005). Initial Conditions to Cosmological N-Body Simulations, or, How to Run an Ensemble of Simulations. *Astrophysical Journal*, 634(2):728–743.
- Zel'Dovich, Y. B. (1970). Gravitational instability: an approximate theory for large density perturbations. *Astronomy & Astrophysics*, 500:13–18.